Electronic supplementary information (ESI)

Construction of Negative Electrostatic Sugared Gourd Pore within Nickel-based Metal-Organic Framework for One-Step Purification Acetylene from Ethylene and Carbon Dioxide Mixture

Xing-Zhe Guo [1, #], Lin Bing [1, #], Guang-Zu Xiong [1, #], Rajamani Krishna [3], Zhao-Rong Zhang [2], Qing-Zan Liu [2], Zhi-Xiong Zhang [2], Liming Fan [4,], Jie Zhang [2,*], Bingwen Li [1,*]*

[1]*Shandong Key Laboratory of Biophysics, Institute of Biophysics, College of Chemistry and Chemical Engineering, Dezhou University, Dezhou 253023, P. R. China. E-mail: libingwen@dzu.edu.cn*

[2] *Department of Chemistry and Chemical Engineering, Taiyuan Institute of Technology, Taiyuan 030008, PR China. E-mail: zhangjie@tit.edu.cn*

[3] *Van't Hoff Institutefor Molecular Sciences, University of Amsterdam, Science Park 904, 1098 XH Amsterdam, The Netherlands. E-mail: R.Krishna@uva.nl*

[4] *School of Chemistry and Chemical Engineering, North University of China, Taiyuan 030051, P. R. China. E-mail: limingfan@nuc.edu.cn*

[#] *These authors contributed equally.*

Content of Table

Materials and methods

Crystal data collection and refinement

Calculation details

Table S1 Selected bond lengths [Å] and bond angles [º] for **SGPF-1**.

Table S2 Crystal data and structure refinement for **SGPF-1**.

Fig. S1 The 2D network composed of Ni(II) and NTA (a), the 1D line consisting of Ni(II) and BPE ligand (b).

Fig. S2 The PXRD pattern of **SGPF-1** immersing in various solvent.

Fig. S3 The FT-IR and TGA curve of SGPF-1 and SGPF-1 immersing in different solvents.

Fig. S4 The PXRD pattern of **SGPF-1** immersing in various temperature.

Fig. S5. BET surface area calculation for the SGPF-1 using the simulated isotherm of CO_2 at 195 K. (a) plot of V (1-P/P_0) vs P/P_0 for the determination using the first consistency criterion, (b) the selected linear plot that satisfies the second consistency criterion and the corresponding BET surface area from the linear fit.

Fig. S6 The separation potential Δq of **SGPF-1** for C_2H_2/CO_2 (v/v = 50/50), C_2H_2/C_2H_4 (v/v = 1/99), CO_2/C_2H_4 (v/v = 50/50)

Fig. S7 The separation potential Δq of **SGPF-1** for (a) C_2H_2/CO_2 (v/v = 50/50); (b) C_2H_2/C_2H_4 (v/v = 1/99): (c) CO_2/C_2H_4 (v/v = 50/50): (d) $C_2H_2/C_2H_4/CO_2$ (v/v/v = 25/50/25)

Fig. S8 The cyclic stability test of **SGPF-1** for C_2H_2/CO_2 (v/v=50/25) and $C_2H_2/C_2H_4/CO_2$ (v/v/v = 25/50/25)

Materials and methods

All chemical reagents are commercially available without further purification. IR spectra were measured on a Thermo Fisher IS-50 FT-IR Spectrometer in the range of 400-4000 cm^{-1}. Elemental analyses were carried out on a Vario MACRO cube elemental analyzer. TGA was measured from 25 to 800 ºC on a TA Instrument at a heating rate 10 ºC/min under air atmosphere. X-ray powder diffractions of titled complexes were measured on a Rigaku XtaLAB Synergy PC diffractometer with Cu-Kα radiation over the 2θ range of 5-50° at room temperature. All gas adsorption isotherms were measured on a Quantachrome Autosorb-iQ surface area by the static volume method.

Crystal data collection and refinement

Single-crystal X-ray diffraction data for SGPF-1 were collected on Bruker SMART APEX II with Mo Kα radiation (λ = 0.71073 Å) using the ω -φ scan mode at 293 K. The SAINT programs were used for empirical absorption corrections and data integration [1]. All Crystal structures were solved by direct method and refined by full-matrix least-squares refinements within the ShelXS-2014 and ShelXL-2014 program [2]. All non-hydrogen atoms were refined anisotropically. Hydrogen atoms of the organic ligands were in the geometrically ideal positions and refined using a riding model. The details of the crystal parameters and selected bond lengths and angles are listed in Table S1 and Table S2.

Calculation details

1. Fitting of unary isotherm data

The unary isotherms for C_2H_2, C_2H_4, and CO_2 measured at two different temperatures 273 K, and 298K in SGPF-1 were fitted with excellent accuracy using the dual-site Langmuir model, where we distinguish two distinct adsorption sites A and B:

$$q = \frac{q_{sat,A} b_A p}{1 + b_A p} + \frac{q_{sat,B} b_B p}{1 + b_B p} \tag{S1}$$

In eq (S1), the Langmuir parameters b_A, b_B are both temperature dependent

$$b_A = b_{A0}\exp\left(\frac{E_A}{RT}\right);\quad b_b = b_{B0}\exp\left(\frac{E_B}{RT}\right) \tag{S2}$$

In eq (S2), E_A, E_B are the energy parameters associated with sites A, and B, respectively.

The unary isotherm fit parameters are provided in Table S1.

Table S1. Dual-site Langmuir fits for guest molecules in SGPF-1.

	Site A			Site B		
	$\frac{q_{A,sat}}{\text{mol/kg}}$	$\frac{b_{A0}}{\text{Pa}^{-1}}$	$\frac{E_A}{\text{kJ mol}^{-1}}$	$\frac{q_{B,sat}}{\text{mol/kg}}$	$\frac{b_{B0}}{\text{Pa}^{-1}}$	$\frac{E_B}{\text{kJ mol}^{-1}}$
C_2H_2	1.5	4.276E-14	56.5	1.1	5.667E-18	69
C_2H_4	0.7	9.880E-12	40	0.9	1.229E-13	41
CO_2	1.3	7.795E-11	27.5	1.1	7.931E-11	33.2

An important aspect to note from the parameters in Table S1 is that the saturation capacity of CO_2 is significantly higher than that of C_2H_4. Consequently, the CO_2(1)/C_2H_4(2) selectivity values increase with increasing pressure due to entropy effects that are driven by saturation capacities.[3]

2. Isosteric heat of adsorption

The isosteric heat of adsorption, Q_{st}, is defined as

$$Q_{st} = -RT^2\left(\frac{\partial \ln p}{\partial T}\right)_q \tag{S3}$$

where, the derivative in the right member of eq (S3) is determined at constant adsorbate loading, q. the derivative was determined by analytic differentiation of the combination of eq (S1), eq (S2), and eq (S3).

3. Q_{st} determination for dual-site Langmuir isotherm

We can rewrite eq (S1) as a quadratic polynomial of the pressures:

$$\left(q_{sat,A} + q_{sat,B} - q\right)b_A b_B p^2 + \left(\left(q_{sat,A} - q\right)b_A + \left(q_{sat,B} - q\right)b_B\right)p - q = 0 \tag{S4}$$

In proceeding further it is convenient to define the following two parameters α and β

$$\alpha = \left(q_{sat,A} + q_{sat,B} - q\right) b_A b_B$$
$$\beta = \left(q_{sat,A} - q\right) b_A + \left(q_{sat,B} - q\right) b_B \tag{S5}$$

For any specified loading q, the corresponding pressure is obtained by solving the quadratic equation (S4), yielding

$$p = \frac{-\beta \pm \sqrt{\beta^2 + 4\alpha\, q}}{2\alpha} \tag{S6}$$

Only one of the two solutions in eq (S6) is physically realizable; this is given by

$$p = \frac{-\beta + \sqrt{\beta^2 + 4\alpha\, q}}{2\alpha} = \frac{\sqrt{\beta + 4\alpha\, q} - \beta}{2\alpha} \tag{S7}$$

The natural logarithm of the pressure is therefore

$$\ln p = \ln\left(\sqrt{\beta + 4\alpha\, q} - \beta\right) - \ln 2\alpha \tag{S8}$$

The derivative $\left(\frac{\partial \ln p}{\partial T}\right)_q$, maintaining the loading constant, can be derived as follows

$$\frac{\partial \ln p}{\partial T} = \frac{\partial \ln\left(\sqrt{\beta + 4\alpha\, q} - \beta\right)}{\partial T} - \frac{\partial \ln 2\alpha}{\partial T}$$
$$\frac{\partial \ln p}{\partial T} = \frac{1}{\left(\sqrt{\beta + 4\alpha\, q} - \beta\right)} \frac{\partial\left(\sqrt{\beta + 4\alpha\, q} - \beta\right)}{\partial T} - \frac{1}{2\alpha} \frac{\partial 2\alpha}{\partial T}$$
$$\frac{\partial \ln p}{\partial T} = \frac{1}{\left(\sqrt{\beta + 4\alpha\, q} - \beta\right)} \left(\frac{1}{2\sqrt{\beta^2 + 4\alpha\, q}} \frac{\partial\left(\beta^2 + 4\alpha\, q\right)}{\partial T} - \frac{\partial \beta}{\partial T} \right) - \frac{1}{\alpha} \frac{\partial \alpha}{\partial T} \tag{S9}$$
$$\frac{\partial \ln p}{\partial T} = \frac{1}{\left(\sqrt{\beta^2 + 4\alpha\, q} - \beta\right)} \left(\frac{1}{2\sqrt{\beta^2 + 4\alpha\, q}} \left(\frac{\partial \beta^2}{\partial T} + 4q \frac{\partial \alpha}{\partial T} \right) - \frac{\partial \beta}{\partial T} \right) - \frac{1}{\alpha} \frac{\partial \alpha}{\partial T}$$
$$\frac{\partial \ln p}{\partial T} = \frac{1}{\left(\sqrt{\beta^2 + 4\alpha\, q} - \beta\right)} \left(\frac{1}{2\sqrt{\beta^2 + 4\alpha\, q}} \left(2\beta \frac{\partial \beta}{\partial T} + 4q \frac{\partial \alpha}{\partial T} \right) - \frac{\partial \beta}{\partial T} \right) - \frac{1}{\alpha} \frac{\partial \alpha}{\partial T}$$

The derivatives of α and β with respective to temperature at constant loading q can be obtained as follows

$$\frac{\partial \alpha}{\partial T} = \left(q_{sat,A} + q_{sat,B} - q\right)\frac{\partial \left(b_A b_B\right)}{\partial T}$$
$$\frac{\partial \beta}{\partial T} = \left(q_{sat,A} - q\right)\frac{\partial \left(b_A\right)}{\partial T} + \left(q_{sat,B} - q\right)\frac{\partial \left(b_B\right)}{\partial T} \qquad \text{(S10)}$$

The temperature dependence of the two Langmuir constants b_A and b_B are described by eq (S2). So we derive the following set of relations

$$\frac{\partial b_A}{\partial T} = -b_{A0}\exp\left(\frac{E_A}{T}\right)\frac{E_A}{RT^2}; \quad \frac{\partial b_B}{\partial T} = -b_{B0}\exp\left(\frac{E_B}{T}\right)\frac{E_B}{T^2}$$
$$b_A b_B = b_{A0}b_{B0}\exp\left(\frac{E_A + E_B}{RT}\right) \qquad \text{(S11)}$$
$$\frac{\partial \left(b_A b_B\right)}{\partial T} = -b_{A0}b_{B0}\exp\left(\frac{E_A + E_B}{RT}\right)\frac{E_A + E_B}{RT^2}$$

Combining eqs eq (S3) with (S9), (S10), (S11) allows the explicit determination of the isosteric heat of adsorption Q_{st}.

The values of the isosteric heat of adsorption, Q_{st}, follow the trend $C_2H_2 > C_2H_4 > CO_2$.

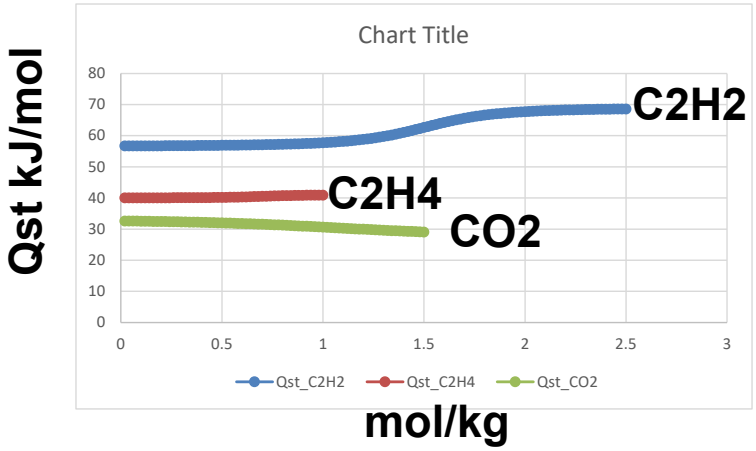

The higher binding strength of C_2H_4 compared to CO_2 explains the CO_2(1)/C_2H_4(2) selectivity trends as determined from the IAST; see below.

4. IAST selectivities

A key metric that quantifies the efficacy of a MOF for separation of binary 50/50 C_2H_2(1)/CO_2(2), 50/50 CO_2(1)/C_2H_4(2), and 1/99 C_2H_2(1)/C_2H_4(2) mixtures is the adsorption selectivity, S_{ads}, defined by

$$S_{ads} = \frac{q_1/q_2}{p_1/p_2} \tag{12}$$

where q_1 and q_2 are the molar loadings of the guest components in the adsorbed phase in equilibrium with a bulk gas phase mixture with partial pressures p_1 and p_2. The mixture adsorption equilibrium is commonly determined using the Ideal Adsorbed Solution theory (IAST)[4] using fits of unary isotherms as input data.

The CO_2(1)/C_2H_4(2) selectivity needs some explanation. At low pressures, the CO_2(1)/C_2H_4(2) is lower than unity. This is because of the slightly larger binding energy of C_2H_4 as seen in the foregoing section. With increasing pressures, the CO_2(1)/C_2H_4(2) selectivity increases to values exceeding unity. The selectivity increase in favor of CO_2 is due to entropy effects caused by the significantly higher saturation capacity of CO_2 as compared to C_2H_4; see Table S1.

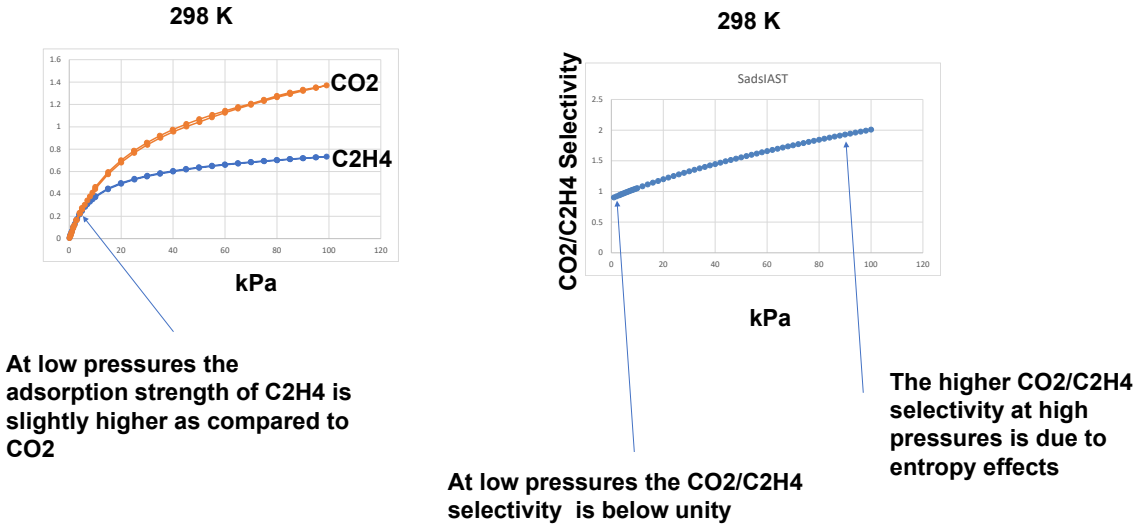

5. Separation potential

For separation of binary 50/50 C_2H_2(1)/CO_2(2), 50/50 CO_2(1)/C_2H_4(2), 1/99 C_2H_2(1)/C_2H_4(2) , and ternary 25/50/25 C_2H_2/CO_2/C_2H_4 mixtures, the maximum productivity of purified product, in the adsorption cycle, that is theoretically achievable in a fixed bed adsorber is determined by the metric defined by Krishna [5,6] as the **separation potential**, Δq , derived on the basis of the shock wave model.

For 50/50 C_2H_2(1)/CO_2(2) mixtures: $\Delta q = \left(q_{C2H2}\right)\frac{50}{50} - q_{CO2}$

For 199 C_2H_2(1)/C_2H_4(2) mixtures: $\Delta q = \left(q_{C2H2}\right)\frac{99}{1} - q_{C2H4}$

For 50/50 CO_2(1)/C_2H_4(2) mixtures: $\Delta q = \left(q_{CO2}\right)\frac{50}{50} - q_{C2H4}$

For ternary 25/50/25 C_2H_2/C_2H_4/CO_2 mixtures: $\Delta q = \left(q_{C2H2} + q_{CO2}\right)\frac{50}{25+25} - q_{C2H4}$

6. Transient breakthrough experiments vs simulations

Transient breakthrough simulations were carried out for binary 50/50 C_2H_2(1)/CO_2(2), 50/50 CO_2(1)/C_2H_4(2), 1/99 C_2H_2(1)/C_2H_4(2) , and ternary 25/25/50 C_2H_2/CO_2/C_2H_4 feed mixtures at 298 K and 100 kPa total pressure using SGPF-1. The simulation methodology is described in earlier work.[5-11] In these simulations, the intra-crystalline diffusional influences are considered to be of negligible importance for each guest.

The bed dimensions and operating conditions are the same as in the experiments: length of packed bed, L = 55 mm; inside tube diameter = 4 mm; volumetric flow rate of gas mixture at the entrance to the bed = 2 mL min^{-1}; mass of SGPF-1 in packed tube = 550 mg. There is reasonable match between experiments and simulations for all mixtures.

7. Density-functional theory (DFT) and GCMC calculations

DFT calculations were carried out using the CP2K code. A mixed Gaussian and planewave basis sets were employed to the calculations. Core electrons were represented with norm-conserving Goedecker-Teter-Hutter pseudopotentials, and the valence electron wavefunction was expanded in a double-zeta basis set with polarization functions along with an auxiliary plane wave basis set with an energy cutoff of 400 Ry. The generalized gradient approximation exchange-correlation functional of Perdew, Burke, and Enzerhof (PBE) was used. Each configuration was optimized with the OT algorithm with the Broyden-Fletcher-Goldfarb-Shanno (BGFS) algorithm with SCF convergence criteria of 3×10^{-6} au. To compensate the long-range van der Waals dispersion interaction between the adsorbate and the MOFs, the DFT-D3 scheme with an empirical damped potential term was added into the energies obtained from exchange-correlation functional in all calculations. The supercell of SGPF-1 was modeled using 2 × 1 × 1 unit cell.

Molecular geometries of all complexes were optimized at the B3LYP level of density functional theory. [12-15] The effective core potential (ECP) of Hay and Wadt with double-ζ LANL2DZ [16] was chosen to describe Ni atoms. For other main group atoms C, O, N, and H, the 6-31g(d,p) basis set [17] was used. Frequency calculations at the same level of theory were also performed to identify all the stationary points as minima (zero imaginary frequencies) and to provide the thermal correction to free energies at 298.15 K and 1 atm. All the DFT calculations were performed with Gaussian 09 packages. [18] The ESP charges were applied to the C2H2, CO2, C2H4, and the smallest MOFs unit.

To calculate adsorption performance in SGPF-1, we use the GCMC simulation method within RASPA package [19]. During the simulation, the MOF are treated as rigid framework and the Generic MOFs force field is used [20]. As for the gas molecules, the potential parameters are taken from TraPPE force field. A cutoff distance is set to 12 Å for the Lennard-Jones (LJ) interactions, and all unit cells were sufficiently replicated to avoid interaction between periodic replica. The long-range electrostatic interactions are treated with CoulombSmoothed algorithm. For each state point, GCMC simulations consist of 100000 steps to ensure the equilibration, followed by 100000 steps to sample the desired thermodynamic properties. The resulting file is processed and analyzed by vislt.

8. Notation

b	Langmuir constant, Pa^{-1}
E	energy parameter, J mol^{-1}
q	component molar loading of species i, mol kg^{-1}
q_{sat}	saturation loading, mol kg^{-1}
Δq	separation potential, mol kg^{-1}
Q_{st}	isosteric heat of adsorption, J mol^{-1}
T	absolute temperature, K

Table S1 Crystal data and structure refinements for SGPF-1.

MOF	SGPF-1
Empirical formula	$C_{78}H_{90}N_8Ni_3O_{30}$
Formula weight	1795.70
Temperature/K	293(2)
Crystal system	trigonal
Space group	R-3
a/Å	15.7490(4)
b/Å	15.7490(4)
c/Å	60.6199(16)
α/°	90
β/°	90
γ/°	120
Volume/Å^3	13021.2(7)
Z	6
ρ_{calc}g/cm^3	1.374
μ/mm^{-1}	0.728
F(000)	5628.0
Crystal size/mm^3	0.18 × 0.16 × 0.12
Radiation	Mo Kα (λ = 0.71073)
2Θ range for data collection/°	4.018 to 59.364
Index ranges	-21 ≤ h ≤ 17, -18 ≤ k ≤ 20, -77 ≤ l ≤ 65
Reflections collected	16699
Independent reflections	7162 [R_{int} = 0.0254, R_{sigma} = 0.0328]
Data/restraints/parameters	7162/0/324
Goodness-of-fit on F^2	1.094
Final R indexes [I>=2σ (I)]	R_1 = 0.0349, wR_2 = 0.0936
Final R indexes [all data]	R_1 = 0.0434, wR_2 = 0.0970
Largest diff. peak/hole / e Å^{-3}	0.45/-0.36
CCDC number	2349983

Table. S2 Selected bond lengths/Å and bond angles/ºfor SGPF-1.

SGPF-1					
Ni1-O	2.0885(12)º	Ni1-O5	2.035(41)º	Ni1-N2	2.108(6)º
Ni1-O4	2.047(61)º	Ni1-O6	2.085(51)º	Ni1-N1	2.096(5)º
O2-Ni1-N9	90.11(5)º	O4-Ni1-O6	86.70(5)º		
O2-Ni1-N1	89.98(5)º	O4-Ni1-N9	87.65(5)º	N2-Ni1-O5[1]	176.59(15)º
O4-Ni1-O2	91.11(5)º	O4-Ni1-N1	91.61(5)º	N2-Ni1-O2	91.14(17)º
O5-Ni1-O4	178.58(5)º	O5-Ni1-O2	90.31(5)º	N1-Ni1-O3	177.20(16)º
O5-Ni1-O6	91.89(5)º	N1-Ni1-O2	90.91(17)º	N1-Ni1-O1	92.05(18)º
O5-Ni1-N9	92.30(5)º	O6-Ni1-O2	176.38(5)º	O6-Ni1-N1	87.20(6)º
O5-Ni1-N1	88.44(5)º	O6-Ni1-N9	92.68(5)º	O6-Ni1-O2	176.38(5)º

Table S3. The detailed comparison of eluted time for the Simulated and experimental breakthrough curves

eluted time / mixture	simulated mixture components			experimental mixture component		
C_2H_2/CO_2 (50/50)	CO_2 9.6 min	C_2H_2 22 min		CO_2 12 min	C_2H_2 24 min	
C_2H_2/C_2H_4 (1/99)	C_2H_4 5.6 min	C_2H_2 57.5 min		C_2H_4 6 min	C_2H_2 44 min	
C_2H_4/CO_2 (50/50)	C_2H_4 6.3 min	CO_2 6.5 min		C_2H_4 5 min	CO_2 11 min	
$C_2H_2/CO_2/C_2H_4$ (25/50/25)	C_2H_4 6.7 min	CO_2 7.9 min	C_2H_2 34 min	C_2H_4 5 min	CO_2 15 min	C_2H_2 26 min

Table S4. The separation performance of selected MOFs at 298 K

	C_2H_2/C_2H_4 (1/99)	C_2H_2/C_2H_4 (50/50)	C_2H_2/CO_2 (50/50)	Refs
ZrT-1-tetrazol	4.05	-	2.83	[28]
FJI-H36	2.40		3.70	[29]
$\{[Fe_3(O)(L)_3]_n(solv)\}_n$	-	1.79	3.59	[30]
$Ti_{0.44}/Ni_{0.56}$-MOF-74	-	4.90	6.80	[31]
L-py-Cu	-	1.74	2.24	[32]
HIAM-111	-	1.62	2.42	[33]
MPM-2	3.90	-	9.00	[34]
Cu-AD-SA	-	3.10	2.50	[35]
NbU-7/NbU-7-Cl	-	-	3.80	[36]
$\{[Co_2(F\text{-}PyIP)_2DMF]$	-	3.30	6.30	[37]
SGPF-1	15.46		7.33	This work

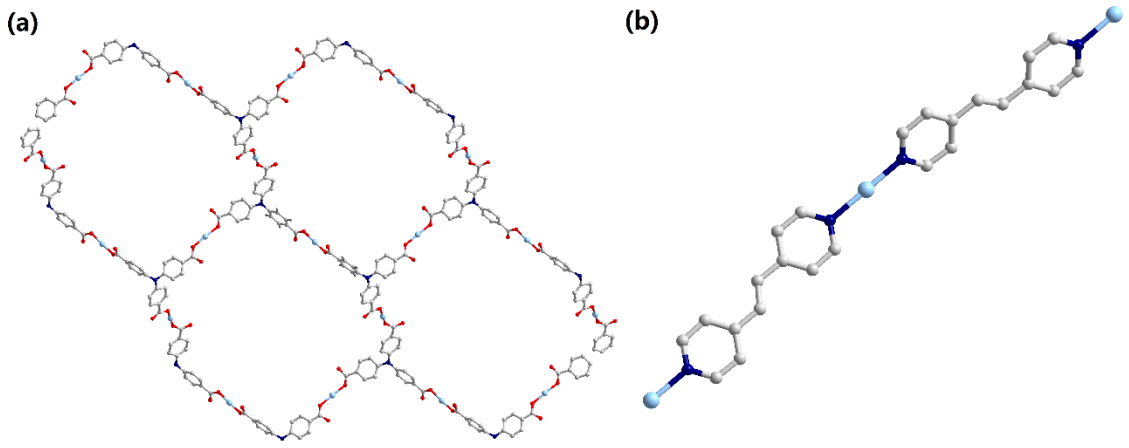

Fig. S1: The 2D network composed of Ni(II) and NTA (a), the 1D line consisting of Ni(II) and BPE ligand (b).

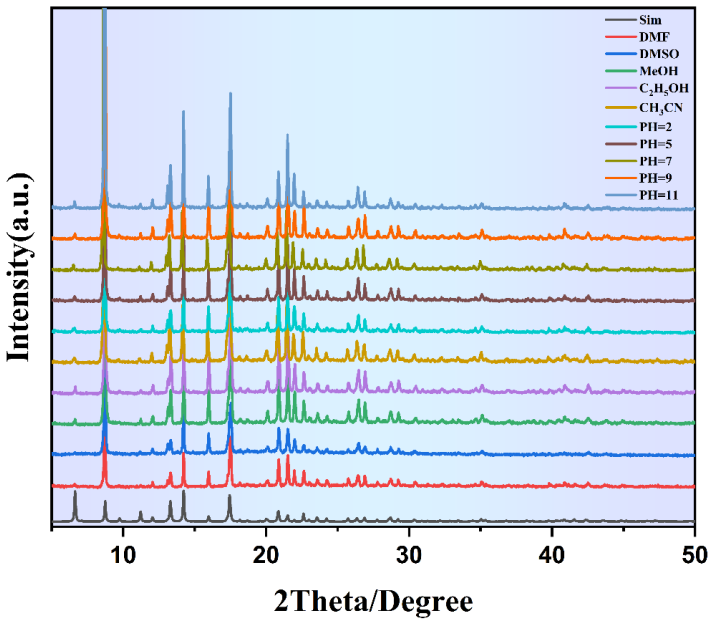

Fig. S2 The PXRD pattern of SGPF-1 immersing in various solvent.

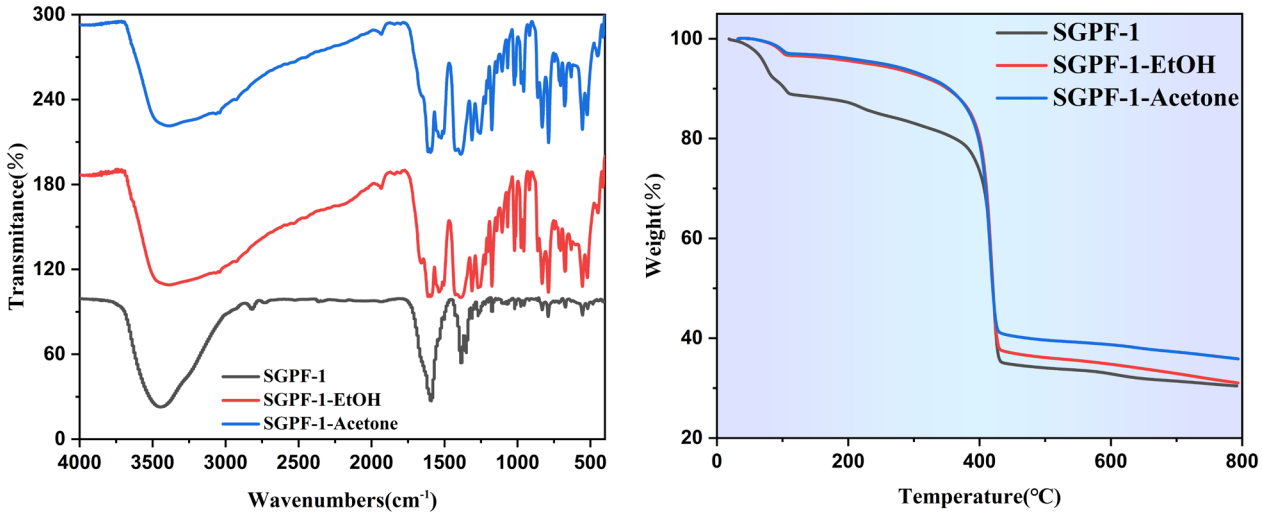

Fig. S3 The FT-IR and TGA curve of SGPF-1 and SGPF-1 immersing in different solvents.

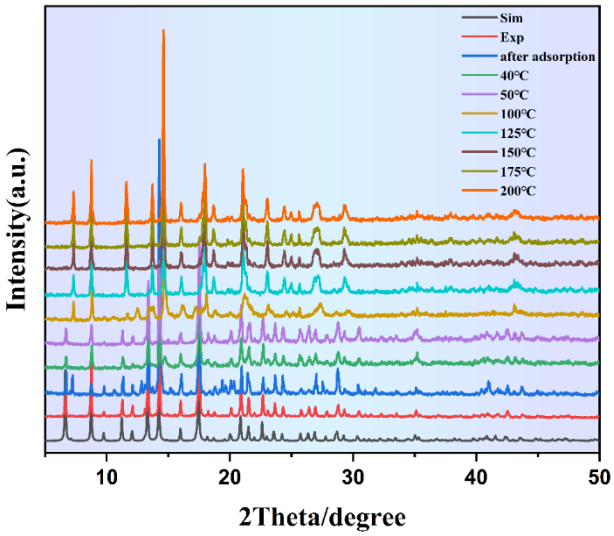

Fig. S4 The PXRD pattern of SGPF-1 immersing in various temperature.

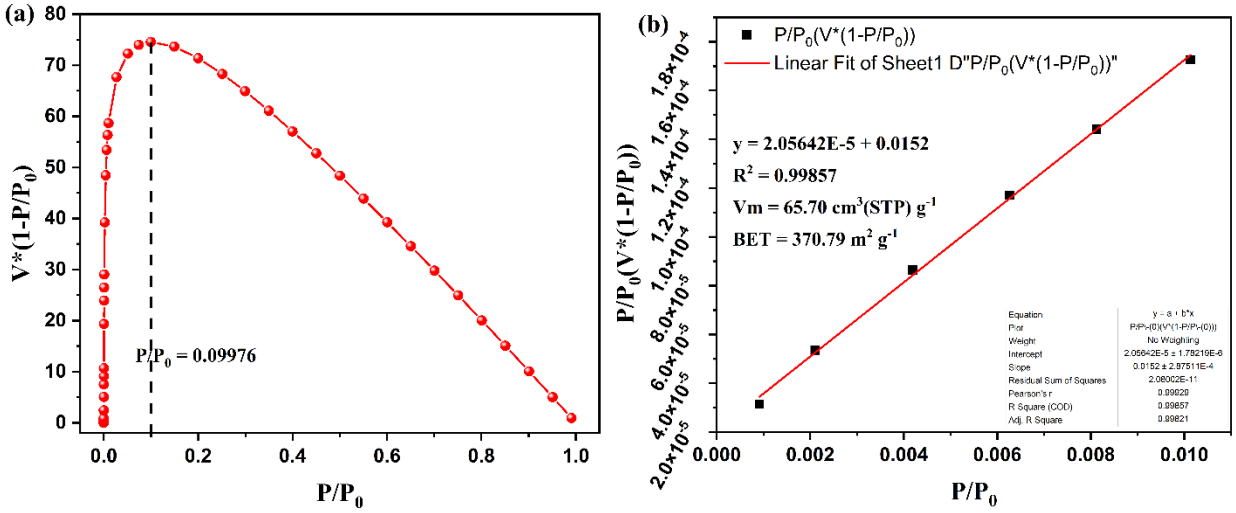

Fig. S5 BET surface area calculation for the SGPF-1 using the simulated isotherm of CO_2 at 195 K. (a) plot of V (1-P/P_0) vs P/P_0 for the determination using the first consistency criterion, (b) the selected linear plot that satisfies the second consistency criterion and the corresponding BET surface area from the linear fit.

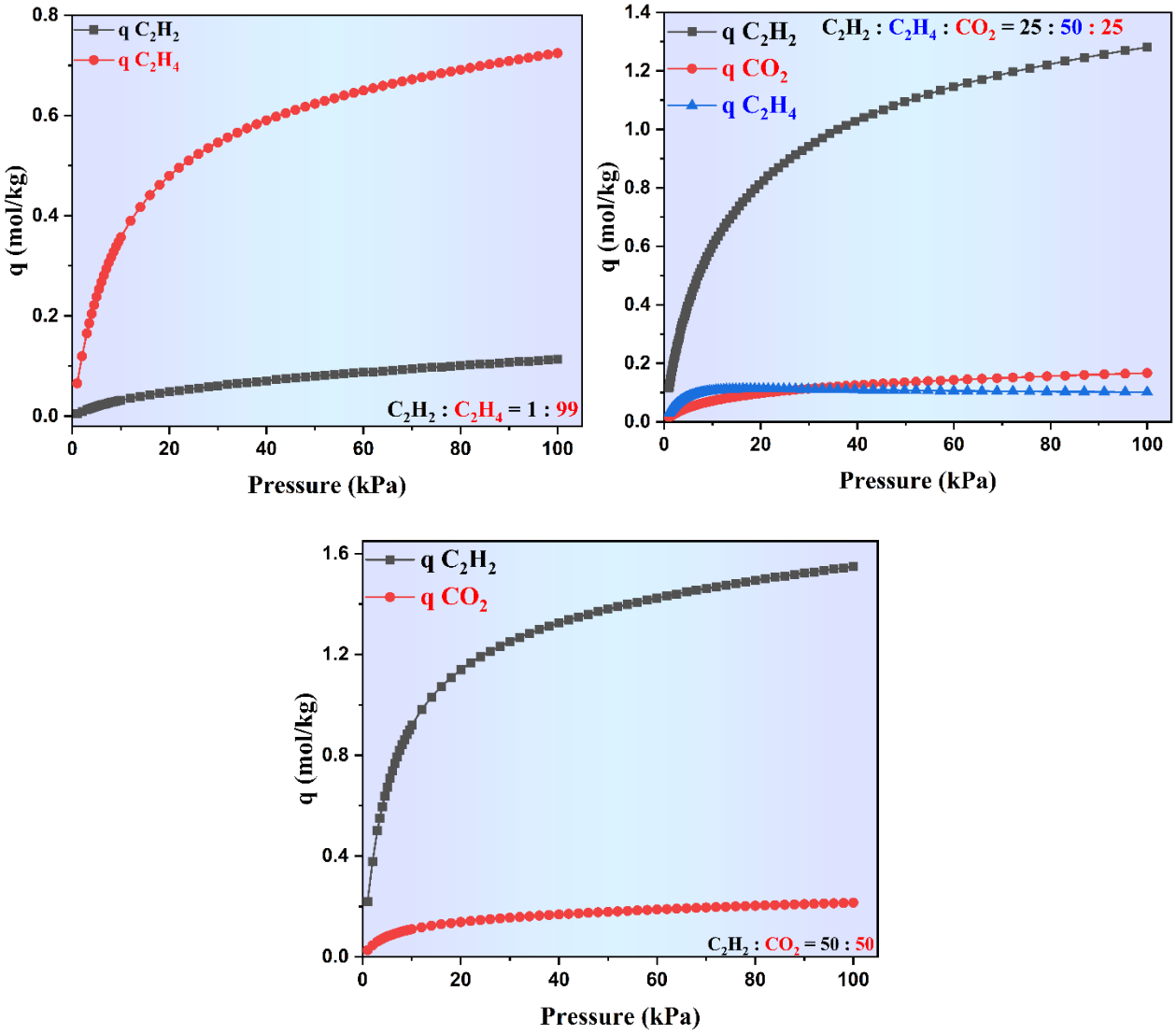

Fig. S6 The separation potential Δq of SGPF-1 for C_2H_2/CO_2 (v/v = 50/50), C_2H_2/C_2H_4 (v/v = 1/99), CO_2/C_2H_4 (v/v = 50/50).

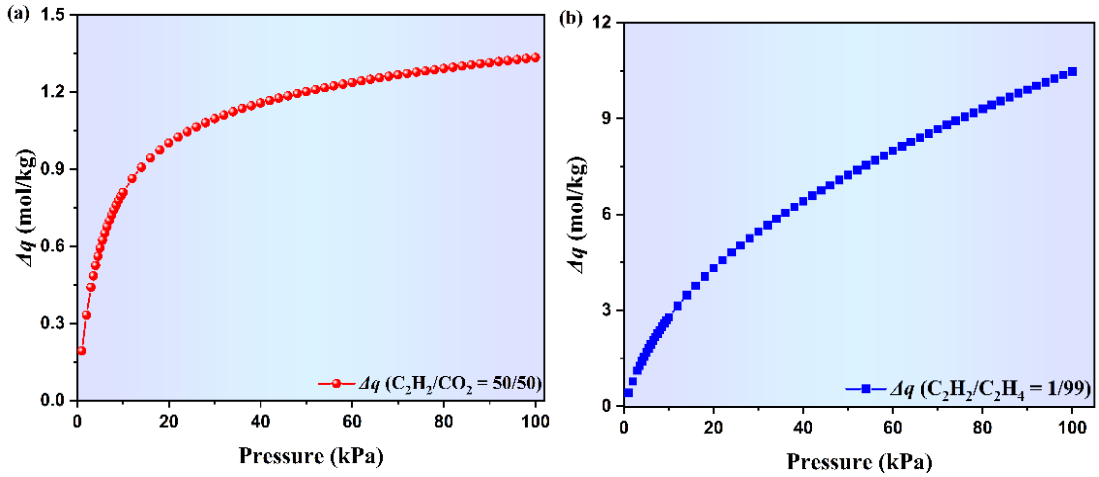

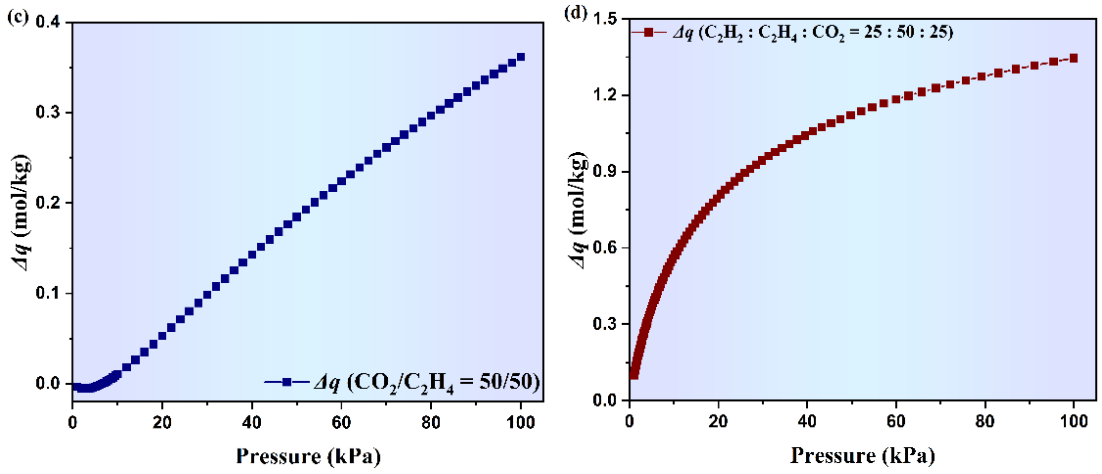

Fig. S7 The separation potential Δq of SGPF-1 for (a) C_2H_2/CO_2 (v/v = 50/50); (b) C_2H_2/C_2H_4 (v/v = 1/99): (c) CO_2/C_2H_4 (v/v = 50/50): (d) $C_2H_2/C_2H_4/CO_2$ (v/v/v = 25/50/25).

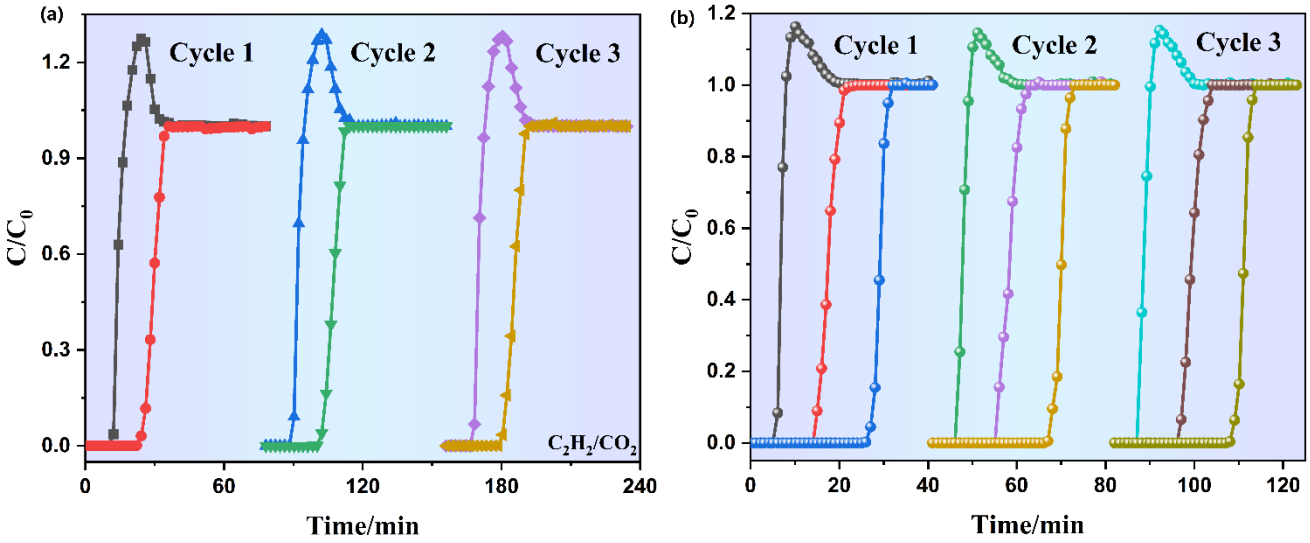

Fig. S8 The cyclic stability test of SGPF-1 for C_2H_2/CO_2 (v/v=50/25) and $C_2H_2/C_2H_4/CO_2$ (v/v/v = 25/50/25).

References

[1] MART & SAINT Software Reference manuals, Version 6.45 (Bruker Analytical X-ray Systems, Inc., Madison, 2003).

[2] G. M. Sheldrick, SHELXL-2014/7. Program for Refinement of Crystal Structures, University of Göttingen: Göttingen, Germany, 2014.

[3] Krishna, R. Elucidation and Characterization of Entropy Effects in Mixture Separations with Micro-porous Crystalline Adsorbents. *Sep. Purif. Technol.* **2019**, *215*, 227-241. https://doi.org/10.1016/j.seppur.2019.01.014.

[4] Myers, A. L.; Prausnitz, J. M. Thermodynamics of Mixed Gas Adsorption. *A.I.Ch.E.J.* **1965**, *11*, 121-130.

[5] Krishna, R. Screening Metal-Organic Frameworks for Mixture Separations in Fixed-Bed Adsorbers using a Combined Selectivity/Capacity Metric. *RSC Adv.* **2017**, *7*, 35724-35737. https://doi.org/10.1039/C7RA07363A.

[6] Krishna, R. Metrics for Evaluation and Screening of Metal-Organic Frameworks for Applications in Mixture Separations. *ACS Omega* **2020**, *5*, 16987−17004. https://doi.org/10.1021/acsomega.0c02218.

[7] Krishna, R. The Maxwell-Stefan Description of Mixture Diffusion in Nanoporous Crystalline Materials. *Microporous Mesoporous Mater.* **2014**, *185*, 30-50. https://doi.org/10.1016/j.micromeso.2013.10.026.

[8] Krishna, R. Methodologies for Evaluation of Metal-Organic Frameworks in Separation Applications. *RSC Adv.* **2015**, *5*, 52269-52295. https://doi.org/10.1039/C5RA07830J.

[9] Krishna, R. Methodologies for Screening and Selection of Crystalline Microporous Materials in Mixture Separations. *Sep. Purif. Technol.* **2018**, *194*, 281-300. https://doi.org/10.1016/j.seppur.2017.11.056

[10] Krishna, R. Synergistic and Antisynergistic Intracrystalline Diffusional Influences on Mixture Separations in Fixed Bed Adsorbers. *Precision Chemistry* **2023**, *1*, 83-93. https://doi.org/10.1021/prechem.2c00003.

[11] Krishna, R. Fundamental Insights into Intra-Crystalline Diffusional Influences on Mixture Separations in Fixed Bed Adsorbers. *Chem Bio Eng* **2024**, *x*, xx. https://doi.org/10.1021/cbe.3c00057.

[12] Becke, A. D. J. Chem. Phys. 1993, 98, 5648.

[13] Stephens, P. J.; Devlin, F. J.; Fnsch, M. J. J. Phys. Chem. 1994, 98, 11623.

[14] Michlich, B.; Savin, A.; Stoll, H.; Preuss, H. Chem. Phys. Lett. 1989, 157, 200.

[15] Lee, C.; Yang, W.; Parr, R. G. Phys. Rev. B 1988, 377, 85.

[16] Knshnan, R.; Binkley, J. S.; Seeger, R.; Pople, J. A. J. Chem. Phys. 1980, 72, 650.

[17] Hariharan, P. C.; Pople, J. A. Theor. Chim. Acta 1973, 28, 213.

[18] Frisch, M.; Trucks, G.; Schlegel, H.; Scuseria, G.; Robb, M.;Cheeseman, J.; Scalmani, G.; Barone, V.; Mennucci, B.; Petersson, G.; Nakatsuji, H.; Caricato, M.; Li, X.; Hratchian, H.; Izmaylov, A.; Bloino, J.; Zheng, G.; Sonnenberg, J.; Hada, M.; Ehara, M.; Toyota, K.; Fukuda, R.; Hasegawa, J.; Ishida, M.; Nakajima, T.; Honda, Y.; Kitao, O.; Nakai, H.; Vreven, T.; Montgomery, J.; Peralta, J.; Ogliaro, F.; Bearpark, M.; Heyd, J.; Brothers, E.; Kudin, K.; Staroverov, V.; Kobayashi, R.; Normand, J.; Raghavachari, K.; Rendell, A.; Burant, J.; Iyengar, S.; Tomasi, J.; Cossi, M.; Rega, N.; Milam, N.; Klene, M.; Knox, J.; Cross, J.; Bskken, V.; Adamo, C.; Jaramillo, J.; Gomperts, R.; Stratmann, R.; Yazyev, O.; Austin, A.; Cammi, R.; Pomelli, C.; Ochterski, J.; Marin, R.; Morokuma, K.; Zakrzewski, V.; Voth, G.; Salvador, P.; Dannenberg, J.; Dapprich, S.; Daniels, A.; Farkas, O.; Foresman, J.; Ortiz, J.; Cioslowski, J.; Fox, D. Gaussian 09, Revision D.01; Gaussian, Inc., Wallingford, CT, 2009.

[19] D. Dubbeldam, S. Calero, D.E. Ellis, R.Q. Snurr, RASPA: Molecular Simulation Software for Adsorption and Diffusion in Flexible Nanoporous Materials, *Mol. Simulat.* **2016**, *42*, 81-101. https://doi.org/10.1080/08927022.2015.1010082.

[20] D. Dubbeldam, K.S. Walton, T.J.H. Vlugt, S. Calero, Design, Parameterization, and Implementation of Atomic Force Fields for Adsorption in Nanoporous Materials, *Adv. Theory Simulat.* **2019**, *2*, 1900135. https://doi.org/10.1002/adts.201900135.